Research Paper

Optimization of Antifouling Properties of Mixed Matrix Membrane Synthesized via In-situ Colloidal Precipitation

Yui Moon Chen [1], Kah Chun Ho [1,*], Mieow Kee Chan [1], Yeit Haan Teow [2], Aida Isma Mohamad Idris [1]

[1] Centre for Water Research, Faculty of Engineering, Built Environment and Information Technology, SEGi University, Jalan Teknologi, Kota Damansara, 47810 Petaling Jaya, Selangor Darul Ehsan, Malaysia
[2] Department of Chemical and Process Engineering, Faculty of Engineering and Built Environment, Universiti Kebangsaan Malaysia, 43600, UKM Bangi, Selangor Darul Ehsan, Malaysia

Article info

Highlights

- MMMs were synthesized via in-situ colloidal precipitation using rGO and MWCNTs
- Quadratic model showed excellent validity and reliability with high R^2
- Normalized flux is known to be strongly influenced by nanomaterials concentration
- Developed quadratic model was satisfactory modelled
- Enhancement of normalized flux at optimized membrane formulation

Graphical abstract

Abstract

This research was conducted to optimize the mixed matrix membrane (MMM) embedded with reduced Graphene oxide/Multiwalled carbon nanotubes (rGO:MWCNTs) by response surface methodology (RSM). The MMMs were fabricated via in-situ colloidal precipitation method. The process variables are concentration of nanomaterials (A) and weight ratio rGO:MWCNT (B), while the response is normalized flux treating methyl orange (MO) dye. The statistical analysis revealed that the experimental result obeyed to the establishment of quadratic model which possessed superior validity and adequacy with high R^2 (0.9249). The normalized flux is known to be strongly influenced by nanomaterials concentration represented by the p-value (0.0004-0.0022< 0.05). The RS plots revealed that the permeate flux and antifouling were attained at minimal concentration of nanomaterials. This is because the adequate dosage of nanomaterials can reduce aggregation and prevent membrane pore blockage. The optimal nanomaterials concentration (0.0303 g/L) and weight ratio (34.3 wt.%) were suggested to achieve high normalized flux of 0.9213. Meanwhile, the confirmatory experiment revealed that the normalized flux of 0.8645 was achieved with low percentage of error 6.16 %. In short, this study asserts that the developed quadratic model was highly reliable in enhancing the normalized flux by optimizing the membrane formulations.
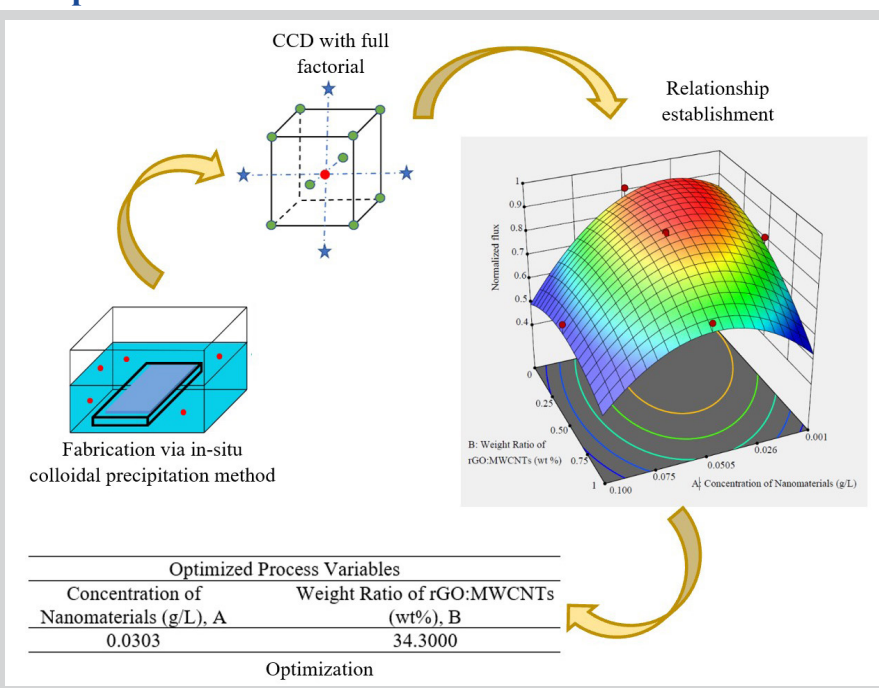
1. Introduction

In Malaysia, one of the fastest-developing industries is the textile industry, as it facilitates economic growth in Malaysia. However, water is utilized extensively in the manufacturing processes of the textile industry, primarily in the dyeing and finishing activities of the plants, and consequently generates a massive volume of dye wastewater [1]. The quantity of dye wastewater released by the textile industry is reaching 900 million tons annually worldwide, ranking sixth among industrial discharge [2]. The improper discharge of untreated dye wastewater into water bodies will result in the aesthetic problem of water bodies and affect the ecosystem of living organisms.

In order to reduce the degree of pollution caused by highly contaminated dye wastewater, dye wastewater treatment is crucial for removing the hazardous materials in wastewater before releasing them to receiving media such as rivers. An integrated system combining coagulation and flocculation with activated sludge biological treatment is one of the conventional treatments. However, the principal disadvantages associated with the conventional system are the highly putrefiable sludge and the high operating costs of chemical addition [3]. Unlike membrane technology, the long processing time of the conventional system is one of the major limitations that affect the treatment efficiency [4]. On the other hand, membrane technology allows the permeate to pass through the finely porous filters while acting as a barrier for large particles or contaminants to pass through the structures. The membrane technology does not require any sophisticated control system in the separation of undesired components from wastewater due to its simple and easy operating procedure [5]. In addition, the membrane technology can be operated at low energy and various scales depending on the requirement [6].

However, the occurrence of membrane fouling declined its efficiency progressively. Membrane fouling is a process whereby the colloidal particles are attached or adsorbed onto the membrane surface due to chemical or physical interaction, resulting in the blockage of fine pores on the membrane. The physical process of removing the foulants such as forward, reverse, and backwashing will destroy the structure of the membrane and shorten its lifespan. Thus, the membrane antifouling properties should be improved through membrane modification to produce a mixed matrix membrane (MMM). The membrane modification can be done by adding the nanomaterials via the *in-situ* colloidal precipitation method to suppress the fouling propensity [7,8]. Some nanomaterials are graphene oxide (GO) and multi-walled carbon nanotubes (MWCNTs). Many studies proved that incorporating GO-MWCNTs can improve separation membrane characteristics and filtration performance. For instance, Ho et al. [9] reported that the synergistic interaction between GO and MWCNTs effectively reduces the fouling propensity of MMM by increasing the normalized flux of membranes in treating high-strength wastewater. This is attributed to the stronger electrostatic repulsion between the negatively-charged colloidal particles and the negatively-charged MMM surface. Moreover, Chae et al. [10] reported that the employment of GO/MWCNTs into the PVDF membrane had enhanced the filtration performance by at least 108% compared to the pure PVDF membrane for water purification purposes. The improvement in filtration performance was attributed to the increased hydrophilicity and membrane pore size which encouraged water penetration through the MMMs. Furthermore, an early study by Zhao et al. [11] proved that the permeability and bovine serum albumin rejection rose significantly by introducing GO/MWCNTs into the membrane matrix. The graphitic carbon materials enhanced the membrane surface morphologies such as porosity and surface roughness which significantly contributed to the membrane performance.

Recently, reduced graphene oxide (rGO) has drawn intensive attention in water treatment and molecular sieving applications owing to their stable and selective 2D channels [12]. Wang et al. [13] reported that the introduction of rGO-MWCNTs into the membrane improved the membrane porosity to form water transfer networks, resulting in excellent transportation of water molecules. This is attributed to the restacking of the rGO nanosheet in rGO/MWCNTs nanocomposite was overcome by the addition of MWCNTs and hence facilitate the water molecules to move through the MMM [14]. However, the concentration of nanomaterials contributes significant influences the membrane performance. The ideal nanomaterials concentration is highly dependent on both the properties of nanomaterials and the membrane composition. Higher concentrations of nanomaterials above the optimal value will lead to the decline of membrane performance due to nanomaterials agglomeration [15]. To produce MMM with optimal antifouling properties, treatment technologies must be developed and process variables must be optimized using statistical analysis. Response surface methodology (RSM) is a set of mathematical and statistical techniques for relating a response to the levels of various input variables or factors that influence it. For instance, Tan et al. [16] used one of the RSM techniques which is central composite design (CCD) to study the effects of adsorption conditions and their interactions on the adsorption efficiency of Congo red dye. In this research, the concentration was found to be important in dye adsorption capacity onto adsorbent, while contact time was found to be less important.

In this study, MMM is developed by incorporating nanomaterials: MWCNTs and rGO in the polyvinylidene difluoride (PVDF) membrane matrix via the *in-situ* colloidal precipitation method. This study evaluates the effect of the weight ratio of rGO: MWCNTs and nanomaterial concentrations. CCD technique is applied in this experiment whereby these parameters will be investigated in five-level: high level (+1), center point (0), and low level (-1). Then, the membrane performance and antifouling properties are evaluated using a dead-end filtration system for treating synthetic methyl orange (MO) solution.

2. Materials and methods

2.1 Materials

rGO nanosheet was employed in membrane modification and obtained from previous research [17]. MWCNTs purity of >97% with a length of <10 μm and diameter of 12-15 nm were obtained from Ugent Tech, Malaysia. N, N-dimethylacetamide (DMAc) (assay GC, area%≥99.0 %) supplied by Merck Co., Germany, was used to dissolve PVDF T-1 (purity of 99.5%) supplied by Shanghai Ofluorine, China. MO with a molecular weight of 327.33 g/mol was purchased from Bendosen, Malaysia.

2.2 Membrane synthesis

PVDF powder was dissolved in DMAc at 65 °C and mechanically agitated at 250 rpm for 4 hours using a hot plate stirrer. The membrane polymer solution was then agitated for additional 4 hours at 40 °C and 250 rpm to guarantee complete polymer dissolution. After that, the membrane polymer solution was placed in a desiccator overnight to eliminate any air bubbles trapped inside it. The rGO/MWCNTs were disseminated in 3 L reverse osmosis (RO) water to produce the coagulation bath. The bath was prepared at nanomaterials concentration (0.001 g/L to 0.1 g/L) and weight ratio of rGO/MWCNTs (0:10 to 10:0) [18]. Then, the coagulation bath of rGO/MWCNTs was treated with ultrasonic irradiation for 30 minutes to boost the nanomaterial's stability in the bath. Then, a flat nonwoven polyester membrane support (CU414 Opti, Neenah US) was slowly poured onto a glass plate with around 25 mL of the membrane polymer solution. With a steady speed of 50 mm/s and a membrane thickness of 200 μm, the casting process was performed with the motorized film applicator and bar coater. The membrane polymer solution film was immersed immediately into the coagulation bath along with the glass plate to prevent solvent evaporation from the thin film surface. Complete phase inversion could be done by allowing the immersion to be left undisturbed for a day.

2.3 Membrane characterization

2.3.1 Functional groups

The existence of functional groups on the membrane was examined by Fourier Transform Infrared (FTIR) Spectrum 100 (Perkin Elmer, UK). The attenuated total reflection (ATR) technique was utilized to determine the changes in a reflected infrared beam when it was in contact with a membrane sample [19]. The operating wave number ranges from 500 cm^{-1} to 4000 cm^{-1}. Equal pressure should be applied to the membrane samples to prevent the differences caused by the pressure and penetrating depth.

2.3.2 Pore size and porosity

The membrane porosity is computed via the gravimetric method in which the liquid mass occupied in membrane pores is determined. In order to ensure water molecules occupied the membrane pores, the membrane sample was submerged in RO water for 12 hours. Next, the membrane sample was cut into 1 cm × 1 cm before weighing. The next step was the drying process of the membrane using an oven (NL Scientific Instruments, Malaysia) at 50 °C for one day to evaporate water occupied within the membrane pores. After drying, the dried membrane sample was weighted. Then, the micro thickness gauge was employed to determine the membrane thickness. The membrane porosity was computed using Equation 1 [20].

$$\varepsilon = \frac{\frac{w_1 - w_2}{\rho_w}}{\frac{w_1 - w_2}{\rho_w} + \frac{w_2}{\rho_p}} \times 100 \tag{1}$$

where ε is membrane porosity (%), w_1 is wet weight of membrane (g), w_2 is dry weight of membrane (g), ρ_w is density of RO water (0.998 g/mL), and ρ_p is density of polymer (density of PVDF is 1.765 g/mL at 25 °C)

Moreover, the filtration velocity method was used to evaluate the membrane mean pore size while the membrane mean pore size was calculated by the Guerout-Elford-Ferry equation as shown in Equation 2 [21].

$$r_m = \sqrt{\frac{(2.9 - 1.75\varepsilon)8\eta lQ}{\varepsilon A \Delta P}} \tag{2}$$

where r_m is membrane mean pore radius (m), ε is membrane porosity (%), η is water viscosity (8.9×10^{-4} Pa.s), l is membrane thickness (m), Q is permeate volume per unit time (m^3/s), A is membrane area (m^2), and ΔP is operational pressure (Pa).

2.3.3 Membrane hydrophilicity

The hydrophilicity of the membrane was determined via contact angle measurement using the contact-angle meter (Attension/KSV Theta, Japan). Firstly, the membrane sample was attached to a flat glass slide with cellophane tape to avoid being positioned at a tilted angle. Subsequently, a water droplet was added to the membrane surface. A high-speed camera with a frequency of 100 pcs/s was utilized to capture the magnified picture of the membrane surface with the dropped water droplets [22]. The contact angle of the membrane surface was accessed by analyzing the series of pictures via OneAttension software. In order to increase the accuracy of data, the contact angle was determined at three different spots.

2.3.4 Membrane zeta potential

A Zeta sizer, Nano-ZS (Malvern instruments Inc., UK) was employed to determine the zeta potential value for membrane surface charge assessment. The membrane sample was prepared in 5 mm × 3.5 mm and placed in the zeta potential cell. Next, a NaCl solution (0.1 mM) with 300–350 nm latex particles at neutral pH was prepared and the membrane sample was immersed in this solution. By inducing an electric field at 25 V/cm, the movement of latex particles at multiple distances away from the membrane surface was determined.

2.3.5 Membrane morphology

Field emission scanning electron microscopy (FESEM) SUPRA 55VP (Zeiss, Germany) was employed to examine the membrane morphology by providing 2D projections in visualizing the topology of the membrane sample.

2.4 Membrane performance evaluation

2.4.1 Permeability

A dead-end membrane filtration system (Amicon, Germany) was utilized to evaluate the membrane permeability. The fabricated membrane was positioned at the bottom of the dead-end cell, with an effective membrane surface area of 13.4 cm^2. To minimize the compaction effect, the pressurization of the membrane was conducted at a constant pressure of 1.5 bar for 20 minutes before the permeability test [23]. Next, the membrane permeate flux was determined by measuring the permeate volume collected over the permeation period by filtering RO water at varied transmembrane pressures (TMPs) of 0.5, 1.0, and 1.5 bar. Equation 3 was employed to compute the membrane permeate flux. Next, the graph of the calculated membrane permeate flux versus TMPs is plotted to determine the permeability indicated by the slope of the graph.

$$J = \frac{\Delta V}{A_e \Delta t} \tag{3}$$

where J is permeate flux (L/m^2·hr), ΔV is permeate volume (L), A_e is effective membrane filtration area (m^2), and Δt is permeation time (hr)

2.4.2 Dye rejection

In order to obtain the dye calibration curve, the MO solution at varying concentrations of 5 mg/L, 10 mg/L, 15 mg/L, and 20 mg/L was prepared by dispersing MO powder into RO water [24]. The absorbance of the dye solution concentration was determined using UV-vis spectroscopy (Shimadzu, Japan) at a maximum wavelength of 484 nm [25]. MO solution containing 20 mg/L was fed into the dead-end membrane filtration system to study the dye rejection. The TMP was fixed at 1 bar throughout the experiment [24]. The permeate concentration was analyzed using the prepared calibration curve. Equation 4 was utilized to compute the dye rejection [26].

$$R = \left(1 - \frac{c_p}{c_f}\right) \times 100 \tag{4}$$

where R is rejection (%), C_p is permeate concentration (mg/L), and C_f is solution concentration (mg/L)

2.4.3 Antifouling

In order to analyze the antifouling properties, the synthesized membrane was placed in the dead-end membrane filtration system with a constant TMP of 1 bar [27]. The feed solution for the dead-end membrane filtration system was the MO solution at 20 mg/L concentration. The filtration duration was fixed at 20 minutes. Equation 5 was then used to compute the normalized flux [28].

$$Normalized\ flux = \frac{J_1}{J} \tag{5}$$

where J_1 is permeate flux of dead-end membrane filtration system and J is pure water flux

2.5 Statistical analysis using central composite design (CCD)

In this study, the statistical analysis of the MMMs was done through Design Expert v13 (Stat-Ease, US). Full factorial was considered where high level (+1), low level (-1), α values of + 1.41421 and -1.41421 with center point (0) were included [29]. The actual values corresponding to their α values were tabulated in Table 1. The Design Expert had designated 13 experimental runs for this research. Table 2 depicts the variables as A: concentration of nanomaterials (g/L) and B: rGO:MWCNTs weight ratio which was expressed as the weight percentage of MWCNTs in nanomaterials (wt %). The pristine membrane was denoted as M0 as it contained no nanomaterials. Normalized flux was the response output determined after membrane performance evaluation. Next, ANOVA was used to evaluate the quality of the fitted model for normalized flux in RSM.

Table 1
Process variables with their coded and actual values

Symbol	Unit	α = -1.41421	-1	0	+1	α = +1.41421
A	g/L	0.001	0.015	0.051	0.086	0.1
B	wt.%	0	14.64	50	85.36	100

Table 2
Experiment run and membrane nomenclature based on CCD

Membrane	Experiment Run	Concentration of Nanomaterials (g/L), A	Weight Ratio of rGO:MWCNTs (wt.%), B
M0	0	0.000	0.00
M7	7	0.001	50.00
M2	2	0.015	14.64
M3	3	0.015	85.36
M9	9	0.051	0.00
M5	5	0.051	50.00
M10	10	0.051	50.00
M11	11	0.051	50.00
M12	12	0.051	50.00
M13	13	0.051	50.00
M1	1	0.051	100.00
M4	4	0.086	14.64
M8	8	0.086	85.36
M6	6	0.100	50.00

2.6 Condition Optimization

The numerical optimization was carried out to maximize the membrane normalized flux at optimum process variables (concentration of nanomaterials, g/L, and the weight ratio of rGO:MWCNTs, wt.%) within the studied range using RSM. To justify the adequacy of the developed model by RSM, a confirmatory experiment was performed to study the effect of the optimized process variables on the membrane-normalized flux. The comparison of the experimental value and the predicted value from RSM was done by computing the percentage of error using Equation 6.

$$Error\ (\%) = \left| \frac{Experimental\ value - Predicted\ value}{Predicted\ value} \right| \times 100\ \% \qquad (6)$$

3. Results and Discussion

3.1 Membrane characterization

3.1.1 Functional groups

Fig. 1 illustrates the analysis of the FTIR on the fabricated membranes (M0, M1, M6, M7, and M9) in this study. The appearance of intense peaks at approximately 1718 cm^{-1} verified the embedment of carbonyl (C=O) groups of rGO/MWCNTs into the membrane matrix via *in-situ* colloidal precipitation. Besides, the presence of alkoxy (C-O) groups is indicated by the absorption peak of 1101 cm^{-1} [30]. Lastly, the peak at 1020 cm^{-1} and 1245 cm^{-1} were observed due to the asymmetric and symmetric vibration of epoxy (C-O-C) groups [31]. The FTIR analysis confirmed the presence of rGO/MWCNTs in the PVDF membrane by the existence of functional groups in the membrane.
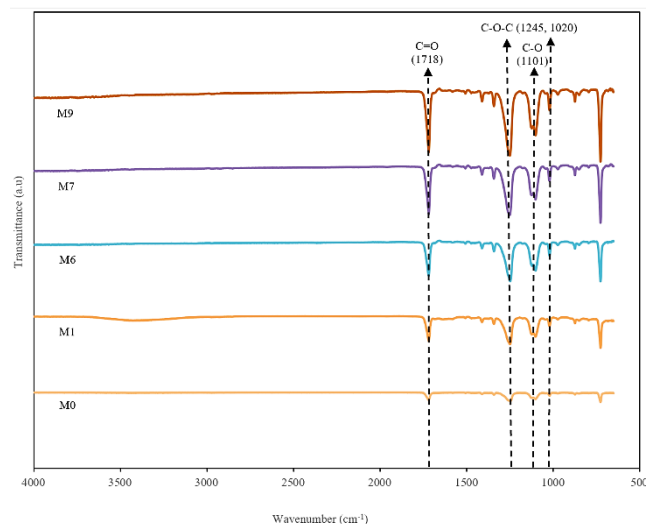

Fig. 1. FTIR analysis for rGO/MWCNT PVDF membranes

3.1.2 Pore size and porosity

Table 3 represents the mean pore size and porosity of the fabricated membranes. The pore size of the pristine M0 membrane is the smallest (15.4 nm). The increment of the mean pore size in MMMs is attributed to the incorporation of nanomaterials that effectively enhance the transfer rate between the solvent and the nonsolvent during the in-situ colloidal precipitation [32]. The accelerated liquid-liquid demixing process subsequently created a larger membrane pore [33]. At a constant weight ratio of rGO:MWCNTs (50%), the mean pore size of MMMs increased drastically from 16.2 nm (M7 membrane) to 40.7 nm (M6 membrane) when the concentration of nanomaterials increased from 0.001 g/L to 0.1 g/L.

Other than that, the employment of MWCNTs was observed to have a major impact on the membrane pore size compared to rGO. For example, at a nanomaterials concentration of 0.051 g/L, the pure MWCNTs membrane (M1 membrane) exhibited a larger mean pore size (36.5 nm) compared to the pure rGO membrane (M9 membrane) with the mean pore size (16.5 nm). This is due to the MWCNTs being richer in hydrophilic functional groups, which can

accelerate the diffusion rate of DMAc and water during the phase inversion process [11].

In addition, the employment of nanomaterials can increase the membrane porosity effectively as revealed in Table 3. For pristine M0 membrane, the porosity is observed to be the lowest amongst the fabricated membrane which is 26.23 %. By comparing M6 and M7 membranes with a constant weight ratio of rGO:MWCNTs (50%), the membrane porosity of the M6 membrane (36.49 %) is higher than M7 membrane (31.16 %) when higher nanomaterials concentration (0.1 g/L) was embedded in M6 membrane.

Table 3
Mean pore size and porosity of the synthesized membranes

Membrane	Mean Pore Size (nm)	Porosity (%)
M0	15.4	26.23
M1	36.5	34.90
M2	23.8	39.85
M3	16.1	36.09
M4	18.7	36.61
M5	29.1	35.50
M6	40.7	36.49
M7	16.2	31.16
M8	49.5	27.81
M9	16.5	34.42
M10	26.6	25.18
M11	26.1	39.00
M12	22.3	45.91
M13	23.5	40.29

3.1.3 Membrane hydrophilicity

Theoretically, the pristine PVDF membrane is established itself as hydrophobic due to the nature of PVDF. Meanwhile, the employment of nanomaterials is aimed at enhancing the hydrophilicity of the membrane surface. The presence of hydrophilic functional groups such as hydroxyl and carbonyl groups in nanomaterials is promoting the membrane hydrophilicity [34]. Nevertheless, a conflictive contact angle measurement was obtained in this study as revealed in Table 4, where the contact angle of pristine M0 membrane is the lowest (64.25°), which implies it behaves more hydrophilic compared to other MMMs. This might be attributed to the emergence of water droplets in the space between the membrane surface and nanomaterials. The formation of water contact angle on the surface of the M0, M2, and M3 membrane was presented in Fig. 2. This phenomenon is also reported by Ho et al. [35] where the mixed-matrix membrane incorporated with GO/OMWCNTs exhibited a higher contact angle using similar *in-situ* colloidal precipitation method. Besides, the increasing trend of water contact angle was observed in the MMMs dominated by rGO. The contact angles of the M2 and M3 membranes are higher than the pristine M0 membrane which are 77.63° and 76.63°, respectively. At a nanomaterials concentration of 0.015 g/L, the M3 membrane containing less rGO content had a lower contact angle (76.63°), while the M2 membrane with higher rGO content had a higher contact angle (77.63°). This is attributed to the lower amount of carboxyl groups on the rGO nanosheet and leads to the formation of an electrostatic attraction along with weaker hydrogen bonding, resulting in higher hydrophobicity than the conventional GO [36].

Table 4
Contact angle of the synthesized membranes

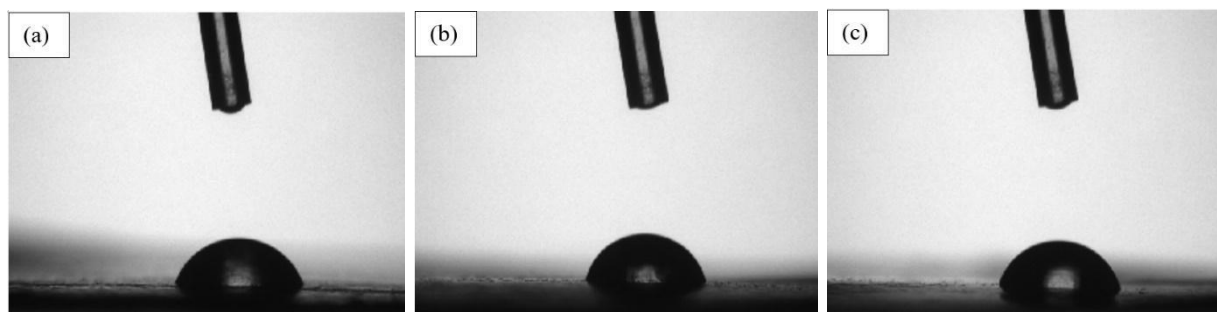| Membrane	Contact Angle (°)
M0	64.25 ± 2.88
M1	77.67 ± 1.35
M2	77.63 ± 2.41
M3	76.63 ± 1.56
M4	77.68 ± 1.52
M5	80.55 ± 2.12
M6	71.21 ± 0.35
M7	70.88 ± 0.79
M8	78.96 ± 2.46
M9	77.97 ± 2.37
M10	86.07 ± 1.92
M11	81.26 ± 2.41
M12	82.63 ± 2.45
M13	82.63 ± 0.74

Fig. 2. Water contact angle of (a) M0, (b) M2, and (c) M3 membrane

3.1.4 Membrane zeta potential

Fig. 3 shows the zeta potential of different membrane sets in this study. It reveals that the zeta potential of the pristine M0 membrane is -11.1 mV which is consistent with the literature [35]. Besides, it is noticeable that the obtained zeta potential for the MMMs became more positive when a higher nanomaterials concentration was used. This could be due to the higher zeta potential of rGO and MWCNTs nanomaterials. For instance, the pure rGO membrane (M9 membrane) has a zeta potential of -0.13 mV, while the pure MWCNTs membrane (M1 membrane) has a zeta potential of -1.3 mV. Hence, adding rGO/MWCNTs into the membrane matrix will induce positive charges to the membrane surface.
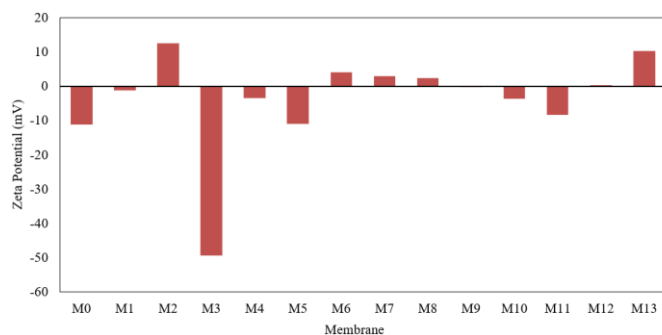

Fig. 3. Zeta potential of the synthesized membranes

3.2 Membrane performance evaluation

3.2.1 Permeability

Fig. 4 shows the permeability of all synthesized membranes in this study. M8 membrane has the highest permeability of 122.25 L/m^2·hr·bar; meanwhile, the pristine M0 membrane has the lowest permeability of 10.801 L/m^2·hr·bar. This is because the M8 membrane has a larger pore size (49.5 nm) and porosity (27.81 %) compared to that of the pristine M0 membrane (15.4 nm and 26.23 %). The presence of nanomaterials (0.086 g/L) in the M8 membrane created larger membrane pore size and porosity, facilitating water permeation through the membrane. At a constant weight ratio of GO:MWCNTs (85.36wt.%), the M3 membrane with a lower concentration of nanomaterials (0.015 g/L) has a lower membrane permeability of (18.982 L/m^2·hr·bar) than that of M8 membrane. Referring to Table 3, the membrane pore size of the M3 membrane is smaller than the M8 membrane, while the former membrane has a higher porosity than the latter membrane. This highlights the importance of membrane porosity in membrane water permeability which is in line with the study by Ali et al. [37]. Fig. 5 represented the FESEM images of M0, M3, and M8 in the topology view. The surface topology proved that the membrane pore size and porosity increased as the concentration of the nanomaterials incorporated into MMMs increased. The enhancement of membrane pore size and porosity encouraged water penetration through the membrane and improved permeability.

By focusing on the weight ratio of nanomaterials, rGO-dominated membranes achieved lower permeability than MWCNTs-dominated membranes. For instance, at a nanomaterials concentration (0.051 g/L), the pure rGO membrane (M9 membrane) has attained a much lower permeability of 18.268 L/m^2·hr·bar compared to that of pure MWCNTs membrane (M1

membrane) of 90.485 L/m^2·hr·bar. This is due to the major portion of the rGO which is hydrophobic as evidenced by its contact angle in Table 4. The hydrophobic membrane is unlikely to attract the water molecules thus weakening water adsorption on the membrane surface eventually hindering the membrane permeability [38].
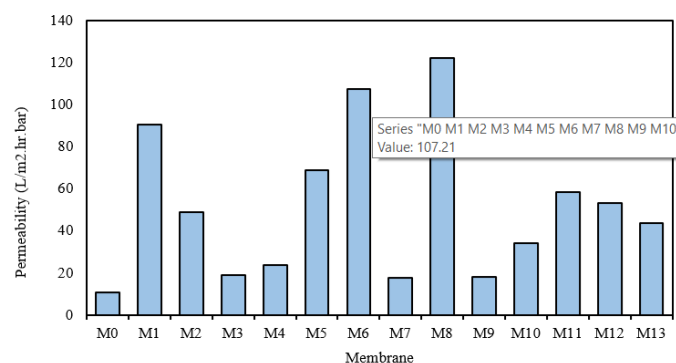

Fig. 4. Permeability of synthesized membranes

3.2.2 Dye rejection

Fig. 6 represents the membrane dye rejection. Pristine M0 membrane has the highest dye rejection (33.97 %) among all the MMMs. This is due to the smallest membrane pore size (15.4 nm) of pristine M0 membrane compared to other membranes. The narrow membrane pore size can retain the MO dye particles with a size range from 6 nm to 8 nm via the size exclusion mechanism [39,40]. On the contrary, the pure MWCNTs membrane (M1 membrane) exhibited the lowest dye rejection (5.65 %) due to its comparatively large pore size (36.5 nm). The employment of MWCNTs enlarged the membrane pore size of the M1 membrane and allowed the MO dye particles to pass through the membrane pores without resistance. Moreover, the M1 membrane captured 1.129 mg/L of MO dye, which was the minimum dye concentration that could be captured by the membrane. This is in line with its lowest rejection behavior. The mechanism of MO dye rejection in ultrafiltration is illustrated in Fig. 7 [41]. Based on Fig. 7, the rejection of MO dye is done by retaining dye particles with larger diameters by the tiny and narrow pores of the membrane.

It is worth pointing out that the membrane dye rejection is influenced by the membrane pore size and the zeta potential of membranes. As seen in Fig. 3, the negative charge of the pristine M0 membrane, represented by its zeta potential (-11.1 mV), can repel the negatively charged MO particles and thus increase the dye rejection [26]. Comparably, the positive surface charge of the M2 membrane (+12.6 mV) tends to attract the MO particles with opposite charges. Due to the strong attractive force between the membrane surface and dye particles, the dye particles tend to deposit on the membrane surface, forming a fouling cake layer. Hence, the dye particles can permeate through the membrane easily, resulting in a lower rejection (5.71 %) in the M2 membrane. In addition, Fig. 8 represents the optical images of the MMM before and after the dye rejection. Based on Fig 8, it can be noticed that the MMM was in white before the dye rejection. After the completion of dye rejection, the color of the MMM changed from white to orange. In other words, the color changes of the dye-captured membrane have proved the attachment of the dye particles on the membrane surface.
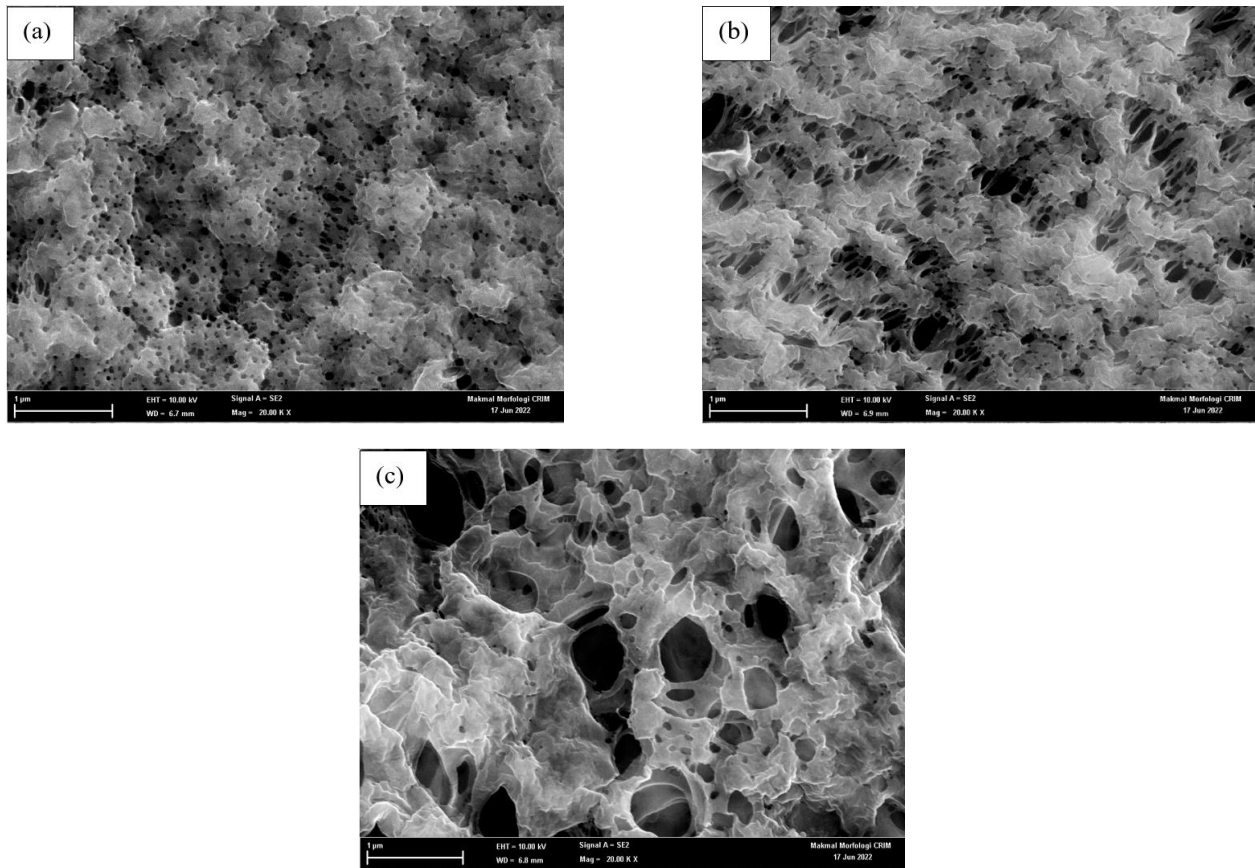
Fig. 5. Topology of (a) M0, (b) M3, and (c) M8 membrane with a magnification of 20 kx
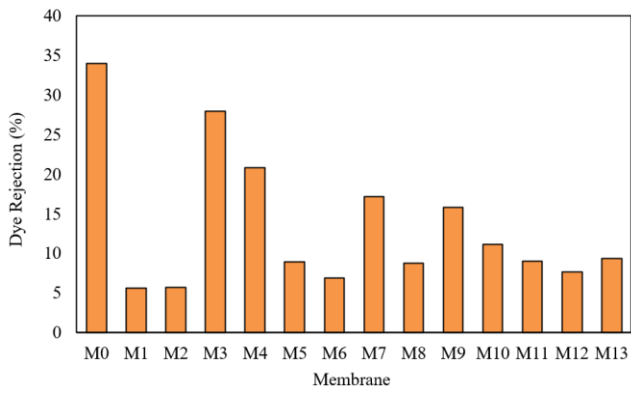

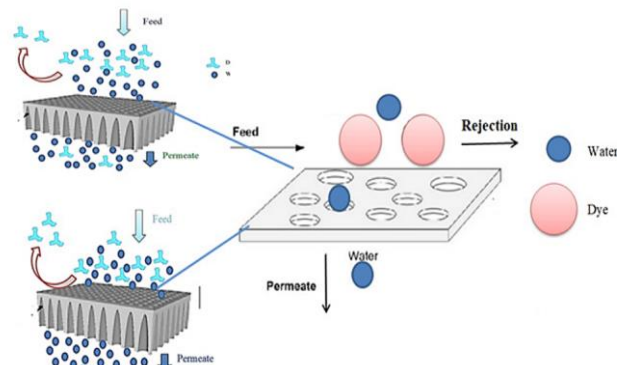**Fig. 6.** Dye rejection of synthesized membranes

Fig. 7. Schematic view of dye rejection in ultrafiltration. Adapted from Ghadhban et al. [41]
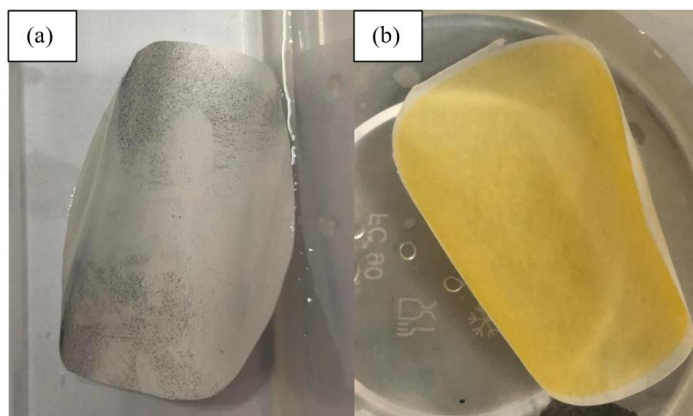

Fig. 8. Optical images of MMM (a) before, and (b) after dye rejection

3.3 Statistical analysis

3.3.1 Antifouling properties of MMMs

The membrane antifouling properties were assessed in terms of normalized flux as illustrated in Table 5. The normalized flux of the pristine M0 membrane and MMMs ranges from 0.609 to 0.9116. The greater the normalized flux, the better the antifouling properties possessed by the membrane. The pristine M0 membrane recorded a higher normalized flux of 0.8554 compared to most MMMs. This is due to the negatively charged membrane surface in the pristine M0 membrane, which is expressed by a zeta potential of -11.1 mV. As a result, a strong electrostatic repulsion force will be formed between foulants and the negatively-charged membrane surface [42]. Thus, the deposition of foulants on the membrane surface can be mitigated.

In terms of the constant weight ratio of GO:MWCNTs (50 wt.%), M6 and M7 membranes which employed the highest (0.1 g/L) and lowest (0.001 g/L) nanomaterial concentrations, the M7 membrane achieved the highest normalized flux (0.9116) whereas the normalized flux of M6 membrane is relatively low (0.6177). This can be validated by the improved pore size and hydrophilicity in the M7 membrane by adding a minute number of nanomaterials (0.001 g/L) as evidenced in Table 3 and Table 4, respectively. Conversely, high nanomaterials content (0.1 g/L) in the M6 membrane is potentially blocking the membrane pores as the aggregation of nanomaterials occurs [43]. Thus, the normalized flux declines significantly as the dye particles cannot pass through the blocked membrane pores.

Furthermore, the result revealed that the MWCNTs significantly impact the normalized flux of MMMs. At a nanomaterial concentration of 0.086 g/L, the M8 membrane with 85.36 wt.% of MWCNTs has achieved a greater normalized flux (0.7476) than that of the M4 membrane (0.609) with 14.64 wt.% of MWCNTs. This can be attributed to the enlarged membrane pore size and hydrophilicity as the introduction of MWCNTs during *in-situ* colloidal precipitation [44]. A similar trend is observed in M2 and M3 membranes with 14.64 wt.% and 85.36 wt.% MWCNTs at constant nanomaterials concentration.

3.3.2 Statistical model for antifouling properties of MMMs

Fig. 9 depicts a 3D graph representing the interlinkage between the process variables and the normalized flux response. The highest normalized flux was observed at low nanomaterials concentration and the low weight ratio of rGO:MWCNTs. A minute amount of rGO/MWCNTs can effectively enhance the membrane surface characteristics such as pore size and hydrophilicity enhancing the membrane antifouling behavior and thus increasing membrane normalized flux. It is noticeable that the normalized flux started to decline when it reached the maximum point as the membrane fouling occurred along with the further increment of nanomaterials concentration and the weight ratio of rGO:MWCNTs. The decline of permeate flux was attributed to the large dosage of nanomaterials tends to cause the nanomaterials agglomeration and thus lead to membrane pore-clogging. Overall, increasing nanomaterials concentration will improve the normalized flux until a certain limit (See red region in Fig. 9); afterward, the flux would decrease due to excessive nanomaterials causing agglomeration.

In addition, Table 6 shows the ANOVA of the quadratic model for the normalized flux of the membrane. Generally, the p-value test in statistical analysis can be used to determine the significance of the model terms. The quadratic model is deemed significant in this study as its p-value smaller than 0.0500 is observed. Several model terms are considered in this quadratic model: A, B, AB, A2, and B2. Based on the p-value shown in Table 6, the significance of the model terms is ranked by p-value as A2 (0.0004), A (0.0022), B (0.0061), B2 (0.0268), and AB (0.1062) which implies that the A2 (p-value = 0.0004) has the most significant effect on improving the membrane normalized flux.

On the contrary, AB with a p-value greater than 0.1000 is considered an insignificant model term in the regression analysis. Besides, the F-value has proven the significance of the developed model as a high F-value (17.25) can only occur due to noise under 0.08 %. Furthermore, the lack of fit F-value (3.83) has indicated that the lack of fit is insignificant relative to the pure error. Overall, this quadratic model delivers high acceptability in this study due to its low p-value (< 0.0500) and high F-value (17.25) as revealed in Table 6.
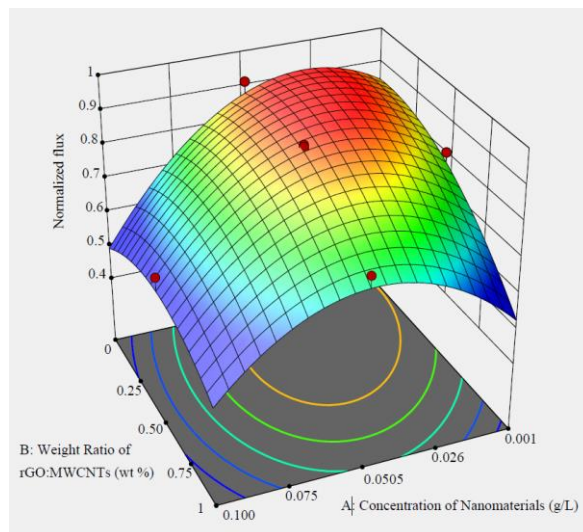

Fig. 9. 3D graph of normalized flux as a function of the concentration of nanomaterials and the weight ratio of rGO:MWCNTs

Table 7 represents the statistical parameters pertaining to the membrane-normalized flux-based model. The statistical parameters such as the coefficient of determination (R^2), adjusted R-squared (R^2_{adj}), and predicted R-squared (R^2_{pred}) are used to assess the reliability of the quadratic models. The developed regression model has been deemed a high-accuracy model due to its high R2 value (0.9249), which is close to unity. Besides, the high reliability of this quadratic model is also shown in the low standard deviation (0.0424) portrayed in Table 7. In addition, the good fit of the regression model can be indicated by the R^2_{pred} and R^2_{adj} with a deviation of lesser than 0.2 [45]. However, the deviation between the R^2_{pred} (0.5736) and R^2_{adj} (0.8713) in this research is 0.3 attributed to the large block effect; therefore, the model reduction should be conducted. Lastly, adequate precision is expressed in the ratio of signal to noise ratio in which a ratio greater than 4 is desired. The adequate signal for this developed model is 11.3561 which is a good indicator of an adequate signal.

The regression model of membrane normalized flux in terms of the actual factors is shown in Equation 7.

$$Y = 0.844563 - 4.9351A - 0.034352B + 3.177709AB + 84.62669 A^2 + 0.359373B^2 \quad (7)$$

Where Y is normalized flux, A is concentration of nanomaterials (g/L), and B is rGO:MWCNTs (wt.%)

Table 5
The normalized flux with the respective variables by CCD.

Membrane	Concentration of Nanomaterials (g/L), A	Weight ratio of rGO:MWCNTs (wt.%), B	Normalized Flux, Y
M0	0.000	0.00	0.8554
M7	0.001	50.00	0.9116
M2	0.015	14.64	0.6472
M3	0.015	85.36	0.6802
M9	0.051	0.00	0.8969
M5	0.051	50.00	0.8065
M10	0.051	50.00	0.8904
M11	0.051	50.00	0.8354
M12	0.051	50.00	0.9054
M13	0.051	50.00	0.8995
M1	0.051	100.00	0.8756
M4	0.086	14.64	0.6090
M8	0.086	85.36	0.7476
M6	0.100	50.00	0.6177

Table 6
ANOVA results for normalized flux

Source	Sum of Squares	DoF	Mean Square	F-value	p-value	
Model	0.1552	5	0.031	17.25	0.0008	significant
A	0.0401	1	0.0401	22.31	0.0022	
B	0.0271	1	0.0271	15.05	0.0061	
AB	0.0062	1	0.0062	3.44	0.1062	
A²	0.0748	1	0.0748	41.56	0.0004	
B²	0.014	1	0.014	7.8	0.0268	
Residual	0.0126	7	0.0018			
Lack of Fit	0.0093	3	0.0031	3.83	0.1137	not significant
Pure Error	0.0033	4	0.0008			
Cor Total	0.1678	12				

Table 7
Statistical parameters pertaining to the normalized flux-based model

Statistical Parameter	Value of Permeate Flux-based Model
R^2	0.9249
R^2_{adj}	0.8713
R^2_{pred}	0.5736
Adequate Precision	11.3561
Standard Deviation	0.0424
Mean	0.7941
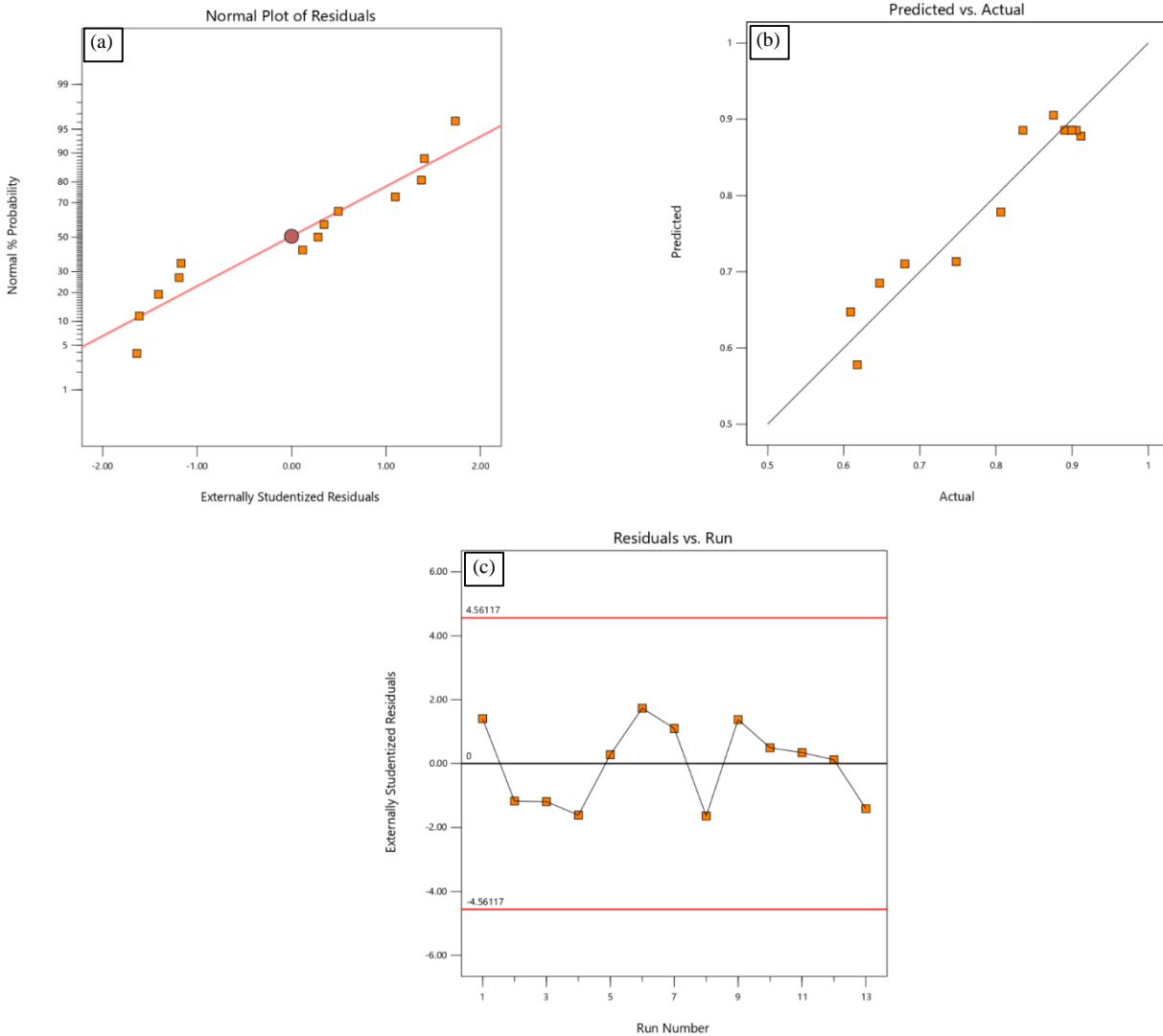
Fig. 10. Plot of (a) normal % probability versus externally studentized residuals, (b) predicted versus actual for normalized flux, and (c) internally studentized residuals versus run number for normalized flux

3.3.3 Verification of regression model on diagnostic plot

The verification of the quadratic model for normalized flux is revealed using three diagnostic plots: normal % probability versus internally studentized residual plot, predicted versus actual values plot, and internally studentized residuals versus number of the runs plot as illustrated in Fig. 10 (a), Fig. 10 (b), and Fig. 10 (c), respectively. The diagnostic plots of the normal % probability of the residuals are used to validate the normal distribution of the actual and predicted values [46]. Fig. 10 (a) verified the normality of the experimental data as most of the residuals were normally distributed which is positioned close to the straight line. Moreover, Fig. 10 (b) represents the distribution of predicted and actual normalized flux. All the points were scattered along the diagonal line. This implies that the developed model equation fits well with the experimental data [47]. Furthermore, Fig. 10 (c) depicts the residuals distributed randomly within the constant range of ± 4.56117 across the graph. This is considered a good indicator of applying constant variance assumption.

3.4 Numerical Optimization

The process variables A (concentration of nanomaterials, g/L) and B (weight ratio of rGO:MWCNTs, wt.%) within the studied range was subjected to numerical optimization for attaining the maximum value of membrane normalized flux. Table 8 shows that the optimized normalized flux of 0.9213 is expected to be achieved at the optimal nanomaterial concentration (0.0303 g/L) and weight ratio (34.3 wt.%) with a desirability of 1. Subsequently, a confirmatory experiment was conducted based on the optimized parameters generated by RSM to verify the optimization experimentally. The outcome of the experiment portraited that the normalized flux achieved 0.8645 at the optimal membrane formulation (0.0303 g/L and 34.3 wt.%). The percentage of error was then computed to affirm the adequacy of the optimization. The percentage of error was determined to be 6.16 % which indicated that the experimental value was in line with the prediction done by RSM.

Table 8
Optimized process variables with the respective predicted response

Optimized Process Variables		Predicted Response	
Concentration of Nanomaterials (g/L), A	Weight Ratio of rGO:MWCNTs (wt.%), B	Normalized Flux	Desirability
0.0303	34.3000	0.9213	1.0000

Conclusion

This study successfully analyzed the antifouling properties of MMMs synthesized via in-situ colloidal precipitation through the statistical analysis tool – RSM. The process variables are concentration of nanomaterials (A) and weight ratio rGO:MWCNT (B), while the response is normalized flux. The experimental data is well-fitted to a quadratic model, and its adequacy and significance were tested statistically via ANOVA. The quadratic model showed superior adequacy and reliability with high R^2 (0.9249) and R^2_{adj} (0.8713). The quadratic model shows that the normalized flux is strongly influenced by process variables A^2 followed by A, B, B^2, and AB. This depicts the significance of nanomaterials concentration (A) in affecting the membrane antifouling properties. The addition of nanomaterials into the membrane matrix via in-situ colloidal precipitation is an effective method to tune the desired membrane characteristics. From the statistical analysis, the concentration of nanomaterials in the coagulation bath should be minimal as a high concentration of nanomaterials in the membrane matrix may lead to aggregation and increase membrane fouling propensity. Moreover, the numerical optimization revealed that the normalized flux can be maximized to 0.9213 at optimum nanomaterials concentration of 0.0303 g/L and the weight ratio of rGO:MWCNTs (34.3 wt.%). The experimental result revealed that the normalized flux attained 0.8645 with a deviation of 6.16 %. This indicated that the similar result between the experimental and predicted values and the quadratic model proved to be highly reliable in optimizing the response. In short, this study asserts that statistical analysis is an excellent tool to evaluate interactions between multiple factors and future studies can focus on the optimization of membrane filtration operating conditions.

CRediT authorship contribution statement

Y.M. Chen: Data curation; Formal analysis; Investigation; Methodology; Writing – original draft.
K.C. Ho: Conceptualization; Funding acquisition; Project administration; Software; Supervision; Writing – review & editing.
M.K. Chan: Funding acquisition; Writing – review & editing.
Y.H. Teow: Funding acquisition.
A. Isma M.I.: Funding acquisition; Writing – review & editing.

Funding

Declaration of Competing Interest

The authors declare that they have no known competing financial interests or personal relationships that could have appeared to influence the work reported in this paper.

Acknowledgments

Abbreviation

ATR	Attenuated Total Reflection
CCD	Central Composite Design
DMAc	Dimethylacetamide
FTIR	Fourier Transform Infrared
GO	Graphene Oxide
MMM	Mixed Matrix Membrane
MO	Methyl Orange
MWCNTs	Multiwalled Carbon Nanotubes
PVDF	Polyvinylidene Difluoride
rGO	Reduced Graphene Oxide
RO	Reverse Osmosis
RSM	Response Surface Methodology

References

[1] F.M. Drumond Chequer, G.A.R. de Oliveira, E.R. Anastacio Ferraz, J. Carvalho, M.V. Boldrin Zanoni, D.P. de Olivier, Textile dyes: dyeing process and environmental impact, Chapter 6, Eco-Friendly Text: Dyeing and Finishing, edited by Günay M. (2013) 151-176. https://doi.org/10.5772/53659.

[2] Q. Liu, Pollution and Treatment of Dye Waste-Water, IOP Conf. Ser. Earth Environ. Sci. 514 (2020) 052001. https://doi.org/10.1088/1755-1315/514/5/052001.

[3] H.R. Lim, C.M. Choo, C.H. Chong, V.L. Wong, Optimization studies for water defluoridation with two-stage coagulation processes using new industrial-based chemical coagulants, J. Water Process Eng. 42 (2021) 102179. https://doi.org/10.1016/j.jwpe.2021.102179.

[4] G. Crini, E. Lichtfouse, Advantages and disadvantages of techniques used for wastewater treatment, Environ. Chem. Lett. 17 (2019) 145–155. https://doi.org/10.1007/s10311-018-0785-9.

[5] N. Wang, X. Li, Y. Yang, Z. Zhou, Y. Shang, X. Zhuang, Photocatalysis-coagulation to control ultrafiltration membrane fouling caused by natural organic matter, J. Clean. Prod. 265 (2020) 121790. https://doi.org/10.1016/j.jclepro.2020.121790.

[6] N.I. Mohamad Mazuki, Y.H. Teow, K.C. Ho, A.W. Mohammad, Techno-economic analysis of single disinfection units and integrated disinfection systems for sewage effluent reclamation, J. Water Process Eng. 36 (2020) 101398. https://doi.org/10.1016/j.jwpe.2020.101398.

[7] W. Xie, J. Li, T. Sun, W. Shang, W. Dong, M. Li, F. Sun, Hydrophilic modification and anti-fouling properties of PVDF membrane via in situ

nano-particle blending, Environ. Sci. Pollut. Res. 25 (2018) 25227–25242. https://doi.org/10.1007/s11356-018-2613-y.

[8] J. Zhang, Z. Wang, M. Liu, F. Zhao, Z. Wu, In-situ modification of PVDF membrane during phase-inversion process using carbon nanosphere sol as coagulation bath for enhancing anti-fouling ability, J. Memb. Sci. 526 (2017) 272–280. https://doi.org/10.1016/j.memsci.2016.12.044.

[9] K.C. Ho, Y.X. Teoh, Y.H. Teow, A.W. Mohammad, Life cycle assessment (LCA) of electrically-enhanced POME filtration: Environmental impacts of conductive-membrane formulation and process operating parameters, J. Environ. Manage. 277 (2021). https://doi.org/10.1016/j.jenvman.2020.111434.

[10] J. Chae, T. Lim, H. Cheng, J. Hu, S. Kim, W. Jung, Graphene oxide and carbon nanotubes-based polyvinylidene fluoride membrane for highly increased water treatment, Nanomaterials. 11 (2021) 2498. https://doi.org/10.3390/nano11102498.

[11] Y. Zhao, Z. Xu, M. Shan, C. Min, B. Zhou, Y. Li, B. Li, L. Liu, X. Qian, Effect of graphite oxide and multi-walled carbon nanotubes on the microstructure and performance of PVDF membranes, Sep. Purif. Technol. 103 (2013) 78–83. https://doi.org/10.1016/j.seppur.2012.10.012.

[12] X.Y. Chen, N. Tien-Binh, A. Romero, A. Patón, L. Sanchez-Silva, J.L. Valverde, S. Kaliaguine, D. Rodrigue, Gas separation properties of mixed matrix membranes based on polyimide and graphite oxide, J. Membr. Sci. Res. 6 (2020) 58–69. https://doi.org/10.22079/JMSR.2019.100069.1244.

[13] Y. Wang, C. Wang, X. Song, S.K. Megarajan, H. Jiang, A facile nanocomposite strategy to fabricate a rGO-MWCNT photothermal layer for efficient water evaporation, J. Mater. Chem. A. 6 (2018) 963–971. https://doi.org/10.1039/c7ta08972d.

[14] A. Kumar, N. Kumar, Y. Sharma, J. Leu, T.Y. Tseng, Synthesis of Free-Standing Flexible rGO/MWCNT Films for Symmetric Supercapacitor Application, Nanoscale Res. Lett. 14 (2019) 266. https://doi.org/10.1186/s11671-019-3100-1.

[15] F. Amiri, A.R. Moghadassi, E. Bagheripour, F. Parvizian, Fabrication and characterization of PES based nanofiltration membrane modified by zeolite nanoparticles for water desalination, J. Membr. Sci. Res. 3 (2017) 50–56. https://dx.doi.org/10.22079/jmsr.2017.23349.

[16] L. Van Tan, N. Thi Hong Tham, V. Thuan Tran, D. Thi To Uyen, P. Van Thinh, Statistical analysis of expanded graphite-decorated cobalt ferrite as adsorbent for removal of Congo Red dye using response surface methodology, Mater. Today Proc. 38 (2020) 2737–2744. https://doi.org/10.1016/j.matpr.2020.08.568.

[17] K.C. Ho, Y.H. Teow, A.W. Mohammad, W.L. Ang, P.H. Lee, Development of graphene oxide (GO)/multi-walled carbon nanotubes (MWCNTs) nanocomposite conductive membranes for electrically enhanced fouling mitigation, J. Memb. Sci. 552 (2018) 189–201. https://doi.org/10.1016/j.memsci.2018.02.001.

[18] Y.H. Teow, A.L. Ahmad, J.K. Lim, B.S. Ooi, Preparation and characterization of PVDF/TiO2mixed matrix membrane via in situ colloidal precipitation method, Desalination. 295 (2012) 61–69. https://doi.org/10.1016/j.desal.2012.03.019.

[19] M.A. Mohamed, J. Jaafar, A.F. Ismail, M.H.D. Othman, M.A. Rahman, Fourier Transform Infrared (FTIR) spectroscopy, Chapter 1, Membrane Characterization, edited by N. Hilal, A.F. Ismail, T. Matsuura, D. Oatley-Radcliffe (2017) 3–29. https://doi.org/10.1016/B978-0-444-63776-5.00001-2.

[20] K.A. Gebru, C. Das, Preparation and characterization of CA−PEG−TiO2 membranes: Effect of PEG and TiO2 on morphology, flux and fouling performance, J. Membr. Sci. Res. 3 (2017) 90–101. https://doi.org/10.22079/jmsr.2016.22820.

[21] L. Ndlwana, K. Sikhwivhilu, R. Moutloali, J.C. Ngila, Heterogeneous Functionalization of Polyethersulfone: A New Approach for pH-Responsive Microfiltration Membranes with Enhanced Antifouling Properties, J. Membr. Sci. Res. 6 (2020) 178–187. https://doi.org/10.22079/JMSR.2019.99706.1238.

[22] M. Chan, S. Ng, Effect of membrane properties on contact angle, AIP Conf. Proc. 2016 (2018) 020035. https://doi.org/10.1063/1.5055437.

[23] W.Y. Pang, A.L. Ahmad, N.D. Zaulkiflee, Antifouling and antibacterial evaluation of ZnO/MWCNT dual nanofiller polyethersulfone mixed matrix membrane, J. Environ. Manage. 249 (2019) 109358. https://doi.org/10.1016/j.jenvman.2019.109358.

[24] C.S. Ooi, M.K. Chan, Nano iron oxide impregnated poly(vinylidene fluoride) ultrafiltration membrane for palm Oil mill effluent treatment, J. Eng. Technol. Adv. 4 (2019) 11–23.

[25] E. Jamshidi, F. Manteghi, Methyl orange adsorption by Fe2O3@Co-Al-layered double hydroxide, Proceedings. 41 (2020) 64. https://doi.org/10.3390/ecsoc-23-06617.

[26] K.C. Ho, S.M. Raffi, Y.H. Teow, Synthesis of MWCNTs/TiO2 photocatalytic nanocomposite membrane via in-situ colloidal precipitation method for methyl orange removal, Int. J. Nanoelectron. Mater. 15 (2022) 207–222.

[27] C. Siang Ooi, M.K. Chan, Nano iron oxide impregnated poly(vinylidene fluoride) ultrafiltration membrane for palm oil mill effluent treatment, J. Eng. Technol. Adv. 4 (2019) 11–23. https://doi.org/10.35934/segi.v4i2.11.

[28] Y.H. Teow, M.S.H. Ghani, W.N.A.W.M. Hamdan, N.A. Rosnan, N.I.M. Mazuki, K.C. Ho, Application of membrane technology towards the reusability of lake water, mine water, and tube well water, J. Kejuruter. 29 (2017) 131–137. https://doi.org/10.17576/jkukm-2017-29(2)-09.

[29] F.Z. Slimane, F. Ellouze, G. Ben Miled, N. Ben Amar, Physical backwash optimization in membrane filtration processes: Seawater ultrafiltration case, J. Membr. Sci. Res. 4 (2018) 63–68. https://doi.org/10.22079/JMSR.2017.66624.1145.

[30] Y. Lin, J. Jin, M. Song, Preparation and characterisation of covalent polymer functionalized graphene oxide, J. Mater. Chem. 21 (2011) 3455–3461. https://doi.org/10.1039/c0jm01859g.

[31] N. Meng, Z. Wang, Z.X. Low, Y. Zhang, H. Wang, X. Zhang, Impact of trace graphene oxide in coagulation bath on morphology and performance of polysulfone ultrafiltration membrane, Sep. Purif. Technol. 147 (2015) 364–371. https://doi.org/10.1016/j.seppur.2015.02.043.

[32] J. Xiong, Y. Gong, C. Ma, X. Zuoiv, J. He, Fabrication and characterization of polyvinylidene fluoride/zinc oxide membranes with antibacterial property, J. Water Supply Res. Technol. - AQUA. 69 (2020) 122–133. https://doi.org/10.2166/aqua.2019.004.

[33] S.S. Hosseini, S. Fakharian Torbati, M.A. Alaei Shahmirzadi, T. Tavangar, Fabrication, characterization, and performance evaluation of polyethersulfone/TiO2 nanocomposite ultrafiltration membranes for produced water treatment, Polym. Adv. Technol. 29 (2018) 2619–2631. https://doi.org/10.1002/pat.4376.

[34] M. Aziz, N.F.T. Arifin, W.J. Lau, Preparation and characterization of improved hydrophilic polyethersulfone/reduced graphene oxide membrane, Malaysian J. Anal. Sci. 23 (2019) 479–487. https://doi.org/10.17576/mjas-2019-2303-12.

[35] K.C. Ho, Y.H. Teow, W.L. Ang, A.W. Mohammad, Novel GO/OMWCNTs mixed-matrix membrane with enhanced antifouling property for palm oil mill effluent treatment, Sep. Purif. Technol. 177 (2017) 337–349. https://doi.org/10.1016/j.seppur.2017.01.014.

[36] C. Cheng, Y. Cai, G. Guan, L. Yeo, D. Wang, Hydrophobic-Force-Driven Removal of Organic Compounds from Water by Reduced Graphene Oxides Generated in Agarose Hydrogels, Angew. Chemie - Int. Ed. 57 (2018) 11177–11181. https://doi.org/10.1002/anie.201803834.

[37] A. Ali, C.L.M. Yu, N.A.M. Sani, M.A.A. Abdullah, M. Awang, N.S. Mohamed, M.A.C. Yunus, Preparation, characterization and performance of polyvinylidene fluoride/tetraoctyl phosphonium bromide nanocomposite ultrafiltration membrane, Malaysian J. Anal. Sci. 22 (2018) 514–521. https://doi.org/10.17576/mjas-2018-2203-20.

[38] H. Qin, K. Fang, Y. Ren, K. Zhang, L. Zhang, X. Zhang, Insights into influences of dye hydrophobicity on cleanliness and resolution of fabric ink-jet printing, ACS Sustain. Chem. Eng. 8 (2020) 17291–17298. https://doi.org/10.1021/acssuschemeng.0c06447.

[39] L. Wu, X. Liu, G. Lv, R. Zhu, L. Tian, M. Liu, Y. Li, W. Rao, T. Liu, L. Liao, Study on the adsorption properties of methyl orange by natural one-dimensional nano-mineral materials with different structures, Sci. Rep. 11 (2021) 10640. https://doi.org/10.1038/s41598-021-90235-1.

[40] A.W. Mohammad, Y.H. Teow, W.C. Chong, K.C. Ho, Hybrid processes: membrane bioreactor, Chapter 13, Membrane Separation Principles and Applications, (2019) 401–470. https://doi.org/10.1016/B978-0-12-812815-2.00013-2.

[41] M.Y. Ghadhban, H.S. Majdi, K.T. Rashid, Q.F. Alsalhy, D.S. Lakshmi, I.K. Salih, A. Figoli, Removal of dye from a leather tanning factory by flat-sheet blend ultrafiltration (UF) membrane, Membranes (Basel). 10 (2020) 47. https://doi.org/10.3390/membranes10030047.

[42] Y.H. Teow, Y.H. Chiah, K.C. Ho, E. Mahmoudi, Treatment of semiconductor-industry wastewater with the application of ceramic membrane and polymeric membrane, J. Clean. Prod. 337 (2022) 130569. https://doi.org/10.1016/j.jclepro.2022.130569.

[43] Y.T. Chung, E. Mahmoudi, A.W. Mohammad, A. Benamor, D. Johnson, N. Hilal, Development of polysulfone-nanohybrid membranes using ZnO-GO composite for enhanced antifouling and antibacterial control, Desalination. 402 (2017) 123–132. https://doi.org/10.1016/j.desal.2016.09.030.

[44] R. Zhou, D. Rana, T. Matsuura, C.Q. Lan, Effects of multi-walled carbon nanotubes (MWCNTs) and integrated MWCNTs/SiO2 nano-additives on PVDF polymeric membranes for vacuum membrane distillation, Sep.

Purif. Technol. 217 (2019) 154–163. https://doi.org/10.1016/j.seppur.2019.02.013.

[45] B. Kim, Y. Choi, J. Choi, Y. Shin, S. Lee, Effect of surfactant on wetting due to fouling in membrane distillation membrane: Application of response surface methodology (RSM) and artificial neural networks (ANN), Korean J. Chem. Eng. 37 (2020) 1-10. https://doi.org/10.1007/s11814-019-0420-x.

[46] H. Asadian, A. Ahmadi, The extraction of gallium from chloride solutions by emulsion liquid membrane: Optimization through response surface methodology, Miner. Eng. 148 (2020) 106207. https://doi.org/10.1016/j.mineng.2020.106207.

[47] N. Shaari, S.K. Kamarudin, Performance of crosslinked sodium alginate/sulfonated graphene oxide as polymer electrolyte membrane in DMFC application: RSM optimization approach, Int. J. Hydrogen Energy. 43 (2018) 22986–23003. https://doi.org/10.1016/j.ijhydene.2018.10.098.